

Flight control of tethered kites in autonomous pumping cycles for airborne wind energy

Michael Erhard*, Hans Strauch

SkySails GmbH, Luisenweg 40, D-20537 Hamburg, Germany

Abstract

Energy harvesting based on tethered kites benefits from exploiting higher wind speeds at higher altitudes. The setup considered in this paper is based on a pumping cycle. It generates energy by winching out at high tether forces, driving an electrical generator while flying crosswind. Then it winches in at a stationary neutral position, thus leaving a net amount of generated energy.

The focus of this paper is put on the flight control design, which implements an accurate direction control towards target points and allows for a flight with an eight-down pattern. An extended overview on the control system approach, as well as details of each element of the flight controller, are presented. The control architecture is motivated by a simple, yet comprehensive model for the kite dynamics.

In addition, winch strategies based on an optimization scheme are presented. In order to demonstrate the real world functionality of the presented algorithms, flight data from a fully automated pumping-cycle operation of a small-scale prototype are given. The setup is based on a 30 m² kite linked to a ground-based 50 kW electrical motor/generator by a single line.

Keywords: Airborne wind energy, Crosswind flight, Flight control, Kite power, Pumping cycle, Tethered kites

1. Introduction

More than thirty years ago [1] energy generation using tethered wings has been proposed for the first time. Since then a great interest in this kind of renewable energy source has emerged, especially during the last decade. The application of tethered wings or kites appear very attractive, as they combine high achievable forces in crosswind flight together with the possibility of easily venturing into higher flight altitudes thereby taking advantage of the higher wind speeds.

The different concepts can be grouped together by using the term 'airborne wind energy', for an overview see e.g. [2]. An extended summary on geometries, theory oriented research activities, realized prototype systems and planned setups can be found in the recent textbook on airborne wind energy [3].

The economic operation of airborne wind energy plants demands for reliable and fully automatic operation of the power generation process. Thus, numerous theoretical control proposals [4, 5, 6, 7, 8] as well as experimental implementations have been published [9, 10, 11, 12]. However, the robust autonomous operation of complete energy production cycles turns out to be quite challenging, especially as optimization of energy output, i.e. performance and robustness, often appear as opposing design prerequisites. Hence, a design process for the control system, which takes into account real world circumstances to the necessary degree, is required. We are convinced, that simplicity, separation of problems and modular structure, grounded in a clear understanding of the physical basis of the controlled plant,

are keys to success in mastering the high perturbations and significant uncertainties, which are inevitably coming along with the natural energy resource wind.

This paper will report on the control system for complete autonomous power cycles with a small-scale 50 kW prototype system using a 30 m² kite. The focus is put on flight control of efficient dynamical pattern-eight trajectories, which are crucial in order to obtain an optimal power generation output. A distinguishing feature of the pattern-eight flight trajectories is the option of flying them in two ways. From the practical point of view, one would prefer the so called eight-down trajectories as those significantly decrease force variability. This allows for a broader operational range of wind conditions and thus increases the average power output. However, the performance advantage comes along with drawbacks of temporarily flying ahead towards the surface and with the need for proper curve flights, which pose special requirements to the flight control system. As a consequence, the previously published control system [9] was extended in order to combine it with target point concepts similar to [12] and [13]. For the overall power generation control, a compact description with three states and simple winch control strategies for the different phases have been added, which already yield remarkable results.

In this manuscript, the complete control design shall be presented, based on the equations of motion of a model [9], which describes the steering behavior of the kite as well as the kinematics, and has been extended for changing tether lengths in [14]. The single design steps towards a robust pattern eight-down flight are discussed in detail and the applicability is illustrated by the discussion of real flight data results.

The paper is organized as follows: starting with a brief sum-

*Corresponding author

Email address: michael.erhard@skysails.de (Michael Erhard)

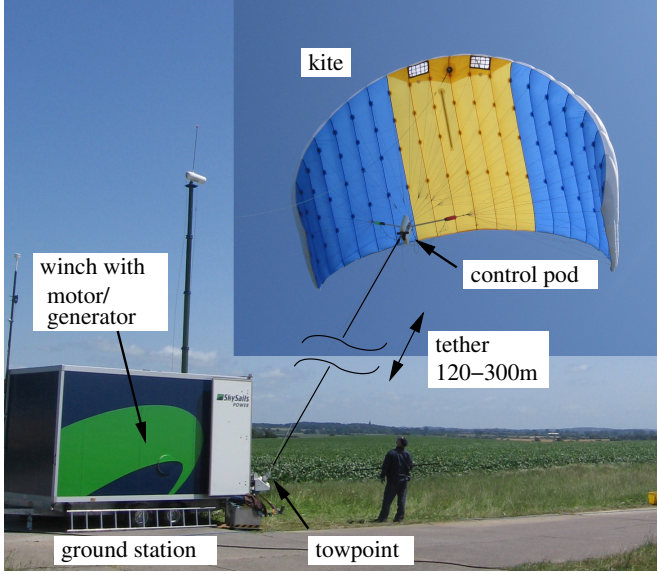


Figure 1: Small scale prototype system for kites of sizes ranging from 20–40 m² (30 m² shown here). The main winch with motor/generator is located in the ground station. A tether line of length typically in the range 150–300 m transfers the forces from the flying system. A distinguishing feature of the latter is the control pod located under the kite, which allows for a single towing rope. The actuator in the control pod pulls certain lines in order to steer the kite.

mary of the system setup and power generation principle in Sect. 2, the pattern eight-down flight and control prerequisites are motivated in Sect. 3. After summarizing the equations of motion in Sect. 4, an overview on the complete control setup is presented in Sect. 5. Sections 6–10 present details of the single controller parts and illustrate their principle of operation by discussing experimental flight data in Sect. 11. A summary and outlook is given in Sect. 12.

2. Implemented prototype and power generation

In this section, a general overview on the architecture and the operation principle for power generation will be given. An extended description of involved components and background information can be found in [15].

2.1. Setup

A picture of the small-scale prototype is shown in Fig. 1. The ram-air kite of 30 m² is controlled by steering lines, which are pulled by an actuator placed in a control pod. The pod is directly located under the kite. This geometry allows for a *single* main towing line, consisting of 6 mm diameter high-performance Dyneema[®] rope, which connects the flying system to the ground station and transfers the aerodynamic forces. The prototype features 300 m of tether length on the main winch, which is attached to a 50 kW electrical motor/generator-combination.

In order to support research and development projects, the prototype is equipped with several sensors. Although the specific choice of sensors and signal preprocessing is important for the whole control design, a detailed discussion would go

Control pod sensors	
ψ_m	Orientation angle w.r.t. wind, determined by a 6-DOF (3 turn rate sensors and 3 accelerometers) inertial measurement unit (IMU) with semiconductor MEMS sensors. The fusion algorithm, based on complementary filtering, also takes into account the wind direction (see below v_w).
$\dot{\psi}_m$	Turn rate around yaw axis measured by the corresponding turn rate sensor of the IMU.
v_a	Air path speed of the flying system measured by a propeller anemometer located at the control pod.
F_{pod}	Tether force measured by a strain gauge.
Ground unit sensors	
φ_m, ϑ_m	Mechanically sensed direction of the tether, referenced to the wind direction (see v_w).
l	Tether length based on rotations of multi-turn encoder attached to the drum.
v_w	Wind speed measured by a 2d ultrasonic anemometer of the ground station, mounted at 5 m altitude. The wind direction is used as reference for the towpoint readings and the inertial measurement unit of the control pod. It is worth mentioning, that an estimation algorithm for the mean wind speed and wind direction at flight altitude may depend on weather conditions. The use of an estimator can significantly improve the robustness and it should be used instead of the anemometer reading. However, even in the latter case the anemometer is still important as initial condition and validation input to the estimator.

Table 1: Overview on sensors and origin of measured values, restricted to quantities discussed in this paper. Proper definitions of the values can be found in the respective sections of the controller description.

beyond the scope of this paper with its emphasis on control. However in order to allow for a proper understanding of the subsequent sections, a short summary on the most important sensors is given in Table 1. For a detailed overview on the sensors for flight control of tethered kites, the interested reader is referred to [16] and to [17], [18] for application examples of fusion algorithms. In the following, measured sensor quantities are indicated by the subscript ‘_m’.

2.2. Power generation cycle

This subsection focuses on the applied principles of power generation. A typical flight trajectory during operation is sketched in Fig. 2. The power generation is done in cycles, which consist of the following three phases:

1. In the *power generation phase*, the kite is flown dynamically in pattern-eight configuration, which induces high line forces. Meanwhile the line is winched out, driving an electrical generator producing energy.
2. When a certain line length is reached, the *transfer phase* brings the kite to a neutral position. The heading is against

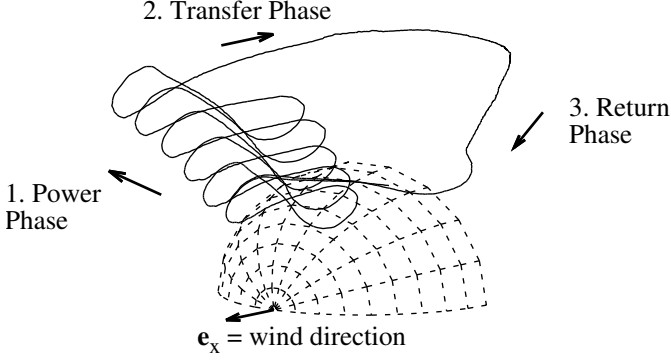


Figure 2: Flight trajectory for the power generation cycle. 3d view of experimental flight data.

the wind resulting in a low line force.

3. During the *return phase*, the line is winched in, operating the generator as motor while the kite is kept at a neutral wind window position. This phase consumes a certain amount of the energy produced in phase 1. As the tether force at neutral position is much lower than during dynamic flight, only a minor fraction of the generated energy of phase 1 is needed leaving a considerable net amount of generated energy. When the lower line length threshold is reached, the whole cycle repeats starting at (1).

This periodic winching process is also called pumping cycle or yo-yo operation configuration.

Finally, it should be remarked that the kite is flown with constant angle of attack during all phases and there is no depowering feature for the return phase implemented as e.g. in [13]. Therefore, the return phase is accomplished by winching the kite directly against the wind. At first sight, this strategy seems to be inefficient as it suggests slow winching speed in order to keep down tether forces. However, rather contrary to intuition, the air flow at the kite, and subsequently the tether forces, are even reduced by increasing the winch speed as shown in Sect. 4.5, making this power generation scheme competitive. The extension of the scheme by variation of the angle of attack would demand for an additional control actuator, which increases complexity and weight of the airborne system. Evaluation of the performance gains versus costs is subject to current theoretical and experimental research activities.

3. Effective power pattern

Effective power generation with tethered kites make use of the huge traction forces, which are generated by dynamical pattern-eight flight. An important distinguishing feature is, that the pattern-eight can be flown in two ways as illustrated in Fig. 3. Note the triangles drawn on the trajectories in the figures indicating the flight directions. Comparing the eight-up and eight-down configurations with respect to maximum energy generation, the eight-down variant is clearly favorable due to the better compensation of gravity by aerodynamic forces as shall be explained in the following. The highest aerodynamic

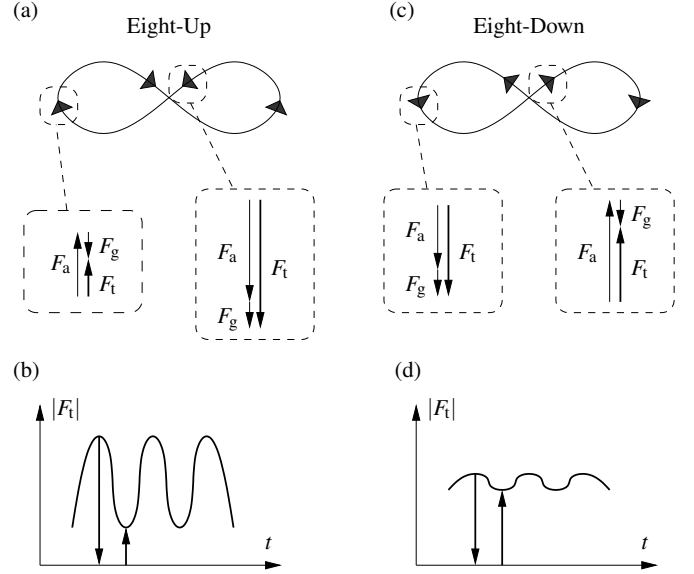


Figure 3: Principle of pattern-eight flight. Note that the eight can be flown in two ways indicated by the triangular shaped arrows on the eight trajectories. The eight-up pattern (a) suffers from low aerodynamic forces F_a in the outer regions further reduced by gravity F_g , leading to low total forces F_t . In the center region, the higher aerodynamic forces are even increased by gravity leading to huge variations of the force with respect to time as shown in (b). For the eight-down variant (c), the variations of gravity and aerodynamic forces compensate partly, leading to a more regular total force, compare (d).

forces occur in the center of the wind window. The eight-up pattern, shown on the left hand side, significantly suffers from flying up against gravity in the outer regions with low aerodynamic forces. In order to improve performance, one can take advantage of gravity in the outer regions with lower aerodynamic forces by flying down and using the high-force region in the center to fly up against gravity. This is achieved by the eight-down pattern shown on the right hand side. A further advantage of these eights-down is the significantly reduced variation in tether force as well as a reduction of the required minimum wind speed for stable operation. Both benefits make the pattern-eight-down concept very attractive for power generation, especially for pumping cycle concepts, based on power generation by winching, which leads to a significant reduction of the apparent wind speed.

Note, that in contrast to eight-ups, which could be controlled by a quite simple approach [9, 14], the given challenge of automated pattern-eight-down flight demands for a certain level of trajectory guidance. We consider the following two properties as essential. First, the flight towards a target point [12] must be controlled quite accurately in order to always keep the kite in the desired region of the wind window and especially in order to compensate for perturbations due to side gusts. Second, the curve flight, which is basically steered by a trapezoidal signal on the actuator, must be well engineered because a major part of the steering speed of the control actuator has to be used explicitly to allow for reasonable small curve radii. In addition, the final target direction of a curve flight should be reached quite accurately with absence of significant overshoots.

Although gravity effects are important for the specific choice

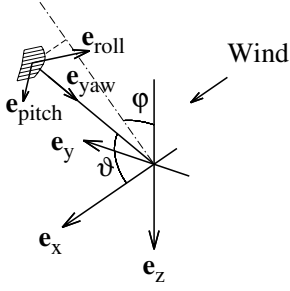


Figure 4: Coordinate system. The distance between origin and kite is given by the tether length l .

of the flight pattern for performance reasons, they are neglected in the following as they could be regarded as uncertainties in the dynamics, which are compensated by the control feedbacks. A thorough modeling in order to cover low wind performance is subject to current research activities and will be published elsewhere.

4. Plant description

In this section, the dynamic model of the system shall be presented. The extended derivation of the model as well as system identification and comparing the model to experimental data is done in [14]. The model is based on four state variables $\mathbf{x} = [\varphi, \vartheta, \psi, l]$ as shown in Fig. 4. The position of the kite \mathbf{r} is given in polar coordinates by the angles φ, ϑ in combination with the tether length l and could be written as

$$\mathbf{r} = l \begin{pmatrix} \cos \vartheta \\ \sin \varphi \sin \vartheta \\ -\cos \varphi \sin \vartheta \end{pmatrix} \quad (1)$$

The orientation of the kite is parameterized by the angle ψ , which could be defined as angle to the wind, i.e. $\psi = 0$ corresponds to a heading directly against the wind. The tether of the model could be regarded as a rigid rod, hence the complete orientation of the kite is determined by the angles φ, ϑ, ψ . An ambient constant and homogeneous wind field with wind speed v_w along the x -direction is assumed.

4.1. Model assumptions

In order to derive the equations of motion, some assumptions are made, which shall be summarized and justified in the following:

- The aerodynamic forces are assumed to be large compared to system masses. This allows for some simplifications. First, the rope can be implemented as simple tether (massless and infinitely thin rod). Second, all acceleration effects can be neglected assuming the system is always in an equilibrium of forces. Especially the latter assumption significantly reduces the equations of motion from second to a first order system.

- The aerodynamics of the kite is reduced to the glide ratio number E , which describes the ratio of the air flow between roll- and yaw axis. Further, it is assumed, that there is no air flow component in pitch-direction (no side-slip).
- The steering behavior of the kite is described by a simple turn-rate law, which has been introduced empirically and shown experimentally [9], [11], but also can be nicely derived from first principles [12].

4.2. Equations of motion

The kite system input is described by the control input vector $\mathbf{u} = [\delta, v_{\text{winch}}]$. The deflection δ determines the steering input applied by the actuator of the control pod to the kite. As winch dynamic is not subject to this paper, it is assumed, that v_{winch} directly determines the change of tether length l .

Taking into account the assumptions of the previous subsection, the following equations of motion can be derived:

$$\dot{\psi} = g_k v_a \delta + \dot{\varphi} \cos \vartheta \quad (2)$$

$$\dot{\vartheta} = \frac{v_a}{l} \left(\cos \psi - \frac{\tan \vartheta}{E} \right) - \frac{\dot{l}}{l} \tan \vartheta \quad (3)$$

$$\dot{\varphi} = -\frac{v_a}{l \sin \vartheta} \sin \psi \quad (4)$$

$$\dot{l} = v_{\text{winch}} \quad (5)$$

The system parameter g_k quantifies the response of the kite due to a steering deflection. The value v_a represents the air path velocity at the kite as it is measured by an on-board anemometer located in the control pod. The same assumptions yield the following relation

$$v_a = v_w E \cos \vartheta - \dot{l} E. \quad (6)$$

In order to get the final result for the complete set of equations of motion, one would usually insert (6) into (2)–(4). This is also done explicitly or implicitly when using these equations for numerical simulations. However, there is a major reason, why this is done only partially here. As we aim at designing a control algorithm for a real system, the capability of reliably measuring certain quantities becomes important, as opposed to a pure simulation. Measuring v_a turns out to be comparably easy by an on-board anemometer in the control pod, while the determination of v_w is quite involved. The straight-forward approach of using an anemometer next to the ground station would require, that the wind field is constant and homogeneous. But this is definitely not the case for airborne wind energy devices making use of higher wind speeds at higher altitudes. Thus, knowing v_a by measurement instead of using (6) could be regarded as kind of generalization of the equations of motion by taking into account local (measured) effects. Hence, using v_a instead of v_w , whenever possible, is preferred in order to enhance the robustness of the control system.

For constant tether lengths $\dot{l} = 0$, it can be shown that $\vartheta \leq \arctan E$ and thus (2)–(4) could be used with v_a as measurement input. However, as soon as winching in is allowed, $\vartheta = \pi/2$ is in the usual operation condition and (3) is no longer defined due to the singularity in $\tan \vartheta$. In order to resolve this issue, (6)

is inserted into (3)–(4). The resulting complete set of equations of motion reads then:

$$\dot{\psi} = g_k v_a \delta + \dot{\varphi} \cos \vartheta \quad (7)$$

$$\dot{\vartheta} = \frac{v_w}{l} (E \cos \vartheta \cos \psi - \sin \vartheta) - \frac{\dot{l}}{l} E \cos \psi \quad (8)$$

$$\dot{\varphi} = -\frac{v_w E \cos \vartheta - \dot{l} E}{l \sin \vartheta} \sin \psi \quad (9)$$

$$\dot{l} = v_{\text{winch}} \quad (10)$$

4.3. Motion on a sphere and crossterm

Due to the motion on a sphere, covering significant angular ranges in short time, the curvature of the state space has certain effects on the kinematics. As the inertial turn-rate sensor is aligned along the yaw axes, one would obtain a turn rate of $\dot{\psi}'_m = 0$ for the tethered motion in absence of other external forces. For a steering deflection, the turn rate is described by the turn-rate law as $\dot{\psi}'_m = g_k v_a \delta$. Comparing this expression to (2)

$$\dot{\psi} = g_k v_a \delta + \dot{\varphi} \cos \vartheta \quad (11)$$

one recognizes the term $\dot{\varphi} \cos \vartheta$, which implements a cross-coupling between ψ and φ, ϑ . This term is defined as crossterm

$$\dot{\psi}_{\text{ct}} \doteq \dot{\varphi} \cos \vartheta \quad (12)$$

Equation (11) then reads

$$\dot{\psi} = \dot{\psi}'_m + \dot{\psi}_{\text{ct}} \quad (13)$$

In other words, the crossterm $\dot{\psi}_{\text{ct}}$ represents the difference between the turn rate w.r.t. the inertial system $\dot{\psi}'_m$ and the time derivative of $\dot{\psi} = d/dt \psi$. Note, that the prime is always used to indicate turn rates w.r.t. an inertial system.

In a cascaded controller topology one would like to setup the chain as $\psi_s \rightarrow \dot{\psi}_s \rightarrow \delta$ and implement both controllers as two cascaded SISO blocks for simplicity and robustness reasons. This could be done by assuming $\dot{\psi}_s \approx \dot{\psi}'_s$, which is an appropriate approximation in some other flight applications. However, for highly dynamical pattern flight, consideration of the crossterm is necessary and can be achieved by using (11) explicitly in the controller design. For simulations $\dot{\psi}_{\text{ct}} = \dot{\varphi} \cos \vartheta$ could be used to accomplish the task. Unfortunately, measuring $\dot{\varphi}$ accurately and reliably turns out to be cumbersome, therefore a quantity based on controller states and sensor values, rather than derivatives of sensor measurements, is preferred. Using the model relation (4) yields:

$$\dot{\psi}_{\text{ct}} = \dot{\varphi} \cos \vartheta = -\frac{v_a}{l \tan \vartheta} \sin \psi \quad (14)$$

Details on controller implementations and performance discussions will be presented in Sect. 7.

4.4. Flight direction

In order to navigate on the sphere, the flight direction γ is defined as follows:

$$\gamma \doteq \arctan(-\dot{\varphi} \sin \vartheta, \dot{\vartheta}) \quad (15)$$

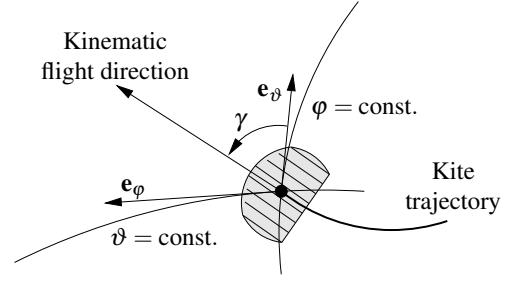


Figure 5: Definition of the flight direction in the spherical coordinate system. The angle γ is defined with respect to the two orthogonal vectors \mathbf{e}_φ and \mathbf{e}_ϑ , which are locally defined by $\vartheta = \text{const.}$ and $\varphi = \text{const.}$, respectively.

As depicted in Fig. 5, γ denotes the angle between the 'latitude' line with $\varphi = \text{const.}$ through the current position \mathbf{r} and the direction of the kinematic motion $\dot{\mathbf{r}}$. Direct measurement of the flight direction is subject to high noise caused by the time derivatives of φ_m and ϑ_m . It is also sensitive to slack line effects in the towing rope. Therefore directly processing γ in a control loop, where γ is computed from sensor values using (15), should be avoided. An alternative is to control the flight direction indirectly by ψ .

In order to obtain the corresponding relation, (8) and (9) are inserted into (15)

$$\gamma = \arctan \left(\sin \psi, \cos \psi - \frac{1}{E} \frac{v_w \sin \vartheta}{(v_w \cos \vartheta - \dot{l})} \right) \quad (16)$$

The inversion of this relation is done by using the relation

$$\psi = \arctan(r \sin \gamma, c_1 + r \cos \gamma) \quad (17)$$

were the quantities r and c_1 can be determined as:

$$c_1 = \frac{1}{E} \frac{v_w \sin \vartheta}{(v_w \cos \vartheta - \dot{l})} \quad (18)$$

$$r = \sqrt{1 - c_1^2 \sin^2 \gamma} - c_1 \cos \gamma \quad (19)$$

The difference between γ and ψ , which is referenced to the air flow $\dot{\mathbf{r}} - \dot{l} \mathbf{e}_{\text{yaw}} - v_w \mathbf{e}_x$, is thus determined by the background wind vector. In crosswind flight with $|\dot{\mathbf{r}}| \gg v_w$, the difference is small compared to the range of directions in the pattern-eight. For an accurate direction control, this difference should be considered, however.

4.5. Winching

In order to examine the effect of winching, the steady state for constant winching speed \dot{l} is calculated by setting $\dot{\vartheta} = 0$ in (8). Some trigonometric manipulations yield for the equilibrium wind window angle

$$\vartheta_0^{(\text{winch})} = \vartheta_0 - \arcsin \left[\frac{\cos \psi}{\sqrt{\cos^2 \psi + (1/E)^2}} \frac{\dot{l}}{v_w} \right] \quad (20)$$

with the zenith position for zero winch speed of $\vartheta_0 = \arctan(E \cos \psi)$. The corresponding curve is shown in Fig. 6.

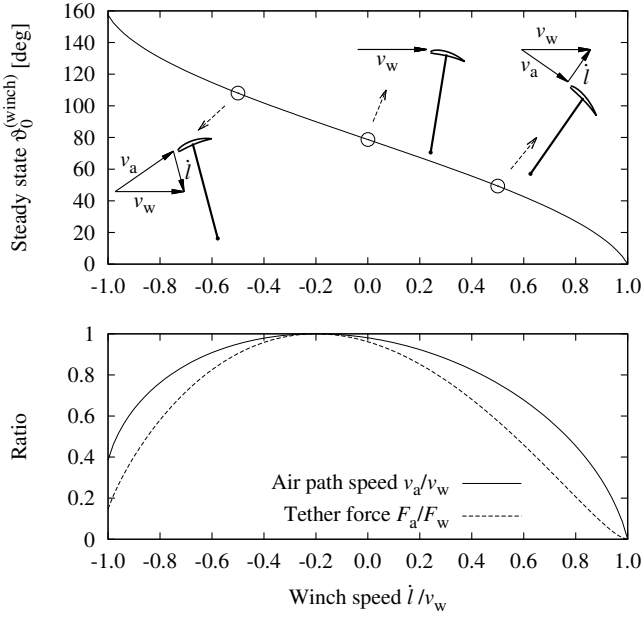


Figure 6: Steady state wind window angle $\theta_0^{(\text{winch})}$ as function of winch speed \dot{l} for $\psi = 0$ and $E = 5.0$ (upper graph). Winching in (out) leads to a increasing (decreasing) wind window angle $\theta_0^{(\text{winch})}$. In the depictive description one obtains a coming forth (falling back) of the kite as indicated by the subfigures for $\dot{l} = \pm 0.5v_w$. The lower figure shows the air path speeds and tether forces, referenced to the ambient wind v_w and the tether force F_w corresponding to an air path speed of v_w . At first sight it is counter-intuitive, that increasing negative winch speeds, while winching in, lead to decreasing tether forces for constant glide ratios. It should be emphasized, that the presented cycle scheme explicitly exploits this feature during the return phase in order to improve the cycle overall power generation efficiency. However, it is worth mentioning the drawback, that negative winch speeds can lead to critical unstable flight situations, if e.g. the winch is stopped suddenly, compare end of Sect. 4.5.

Note, that reeling in at windward position in order to decrease the tether force is explicitly exploited in the cycle scheme presented here.

In order to further illustrate this effect of winching, the side view of a cycle trajectory is plotted in Fig. 7. Finally, a brief comment on the winching-in phase shall be given. In order to keep the kite in a stable flight configuration, a certain minimum air path speed $v_{a,\min}$ is required. Assuming $v_a > v_{a,\min}$ and resolving (6) w.r.t. \dot{l} yields:

$$\dot{l} < -\frac{v_{a,\min}}{E} + v_w \cos \vartheta \quad (21)$$

It can be seen, that for angles $\vartheta > \pi/2$ a certain winch speed $\dot{l} < 0$ is needed in order to keep the stable flight configuration. Before stopping the winch, the angle ϑ has to be reduced by flying into the wind window as is done by starting the power phase. This issue imposes the reliability requirement of 'avoiding sudden stops by all means' to the winch setup.

5. Control design overview

In this section, a brief overview on the complete control system is given. Details of the controller parts and presentation of experimental results will be given in the subsequent sections.

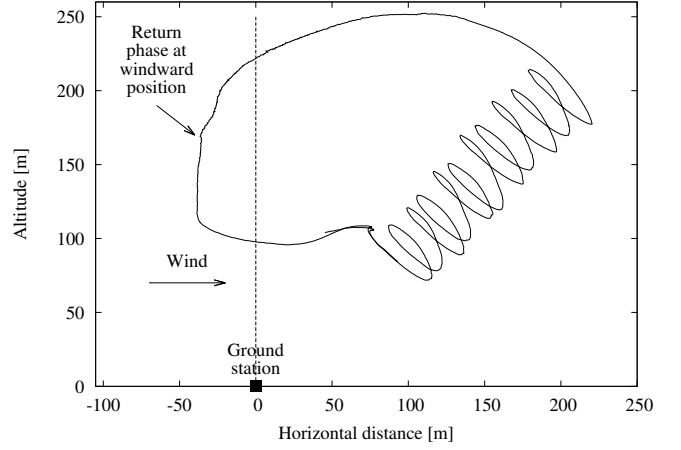


Figure 7: Side view of trajectory for one power cycle. Note, that during the return phase, the kite is flown in a windward position in order to further reduce the tether force, compare Fig. 6.

5.1. Design philosophy

Before diving into the details of the control system, the design ideas and principles are summarized in order to provide a kind of justification for the described setup in the rest of the paper. Examining the equations of motion (2)–(5), a possible control approach could be based on the concept of dynamic inversion or model predictive control [19]. In the field of tethered kite control, such approaches have been applied to much more complex theoretical models [20], [21] than the model of Sect. 4, and the principal functionality has been demonstrated successfully in simulations. However, successful applications of these involved algorithms on real prototypes has not been reported yet.

A prototype setup and the task of developing an operationally robust, commercial control system imposes a different emphasis and leads to a different controller structure. The plant is subject to huge perturbations due to wind gusts with uncertainties about wind conditions over the range of flight altitudes even for one cycle. In order to successfully tackle these real world and industrial challenges, one prefers certain control topologies and design principles, which will be summarized in the following:

- An important step is to split up the system into separate parts which can be described, to a large degree, by analytic equations, related to intuitive physical models. For each subsystem, it is much easier to design robust, but still simple and linear controllers, augmented by nonlinear elements like limiters, which can be easily inserted and tuned. This approach naturally leads to a cascaded controller topology.
- Implement a feedforward/feedback structure in order to achieve the bandwidth needed for tailored curve flight and to capture the major non-linearities in the feedforward path. The feedforward paths also allow for a proper shaping of signals according to system constraints and can be easily added to a cascaded design.

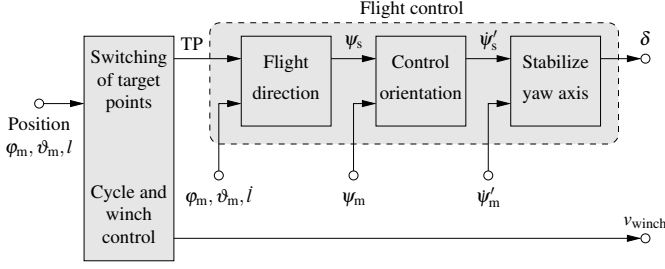


Figure 8: Overview on the control system.

- Modify the open loop dynamics by the feedback to the necessary degree only. As a consequence, we do not try to follow an exact predefined trajectory at all cost. The achievable control bandwidth of the inner loop would not allow for very high accuracy, when taking robustness as major design consideration into account. Instead, the simple target point tracking scheme proposed in [12] was implemented, which supports a kind of natural evolution of the eight-pattern, but keeps the pattern reliably in the desired region of the wind window on the other hand.

The implemented overall control system structure is depicted in Fig. 8. The control strategy is based on flight control towards target points (TPs), while switching to a subsequent target point before the current target point is reached [12]. This algorithm, which also controls the winch, is called *winch and cycle control*. Compared to [12], where a simple heading control has been implemented, we present a cascaded *flight control* setup based on earlier work [9], providing accurate heading control as well as shaped curve flight, which are both prerequisites for robust eight-down flight.

5.2. Winch and cycle control

This part is responsible for the overall control of the power generation cycle and the computation of the winch speed set value v_{winch} .

1. The *cycle control* in its simplest, albeit not fully optimized, version can be based on three target points only. The geometry of these target points is indicated in Fig. 11. Switching between target points is triggered by geometric conditions, i.e. by approaching condition to the active target point as well as based on the line length l in order to obtain the periodic repetitions of cycles consisting of power and return phases. Details will be given in Sect. 9.
2. In order to implement an efficient *winch control* algorithm, the overall optimization problem involving complete cycles has to be tackled as suggested in [22]. However, as wind conditions in different flight altitudes are not exactly known and subject to gusts and significant variations, simpler approaches are desirable at least for first proof-of-concept flight tests. Performing a rudimentary numerical optimization with the model (2–6), a simple relation was identified, which allows for the computation of the winch speed based on the geometric condition of wind window position and wind speed only. Although this approach is

one of the simplest, it is performing surprisingly well as it is capable of operating all phases and the energy production seems not to be much away from the achievable optimum. Details will be given in Sect. 10.

5.3. Flight control

The flight control design is composed of three cascaded controllers as shown in Fig. 8. In the following, these blocks are described from right to left.

1. Inner loop ($\dot{\psi}'$ -controller): Yaw axis stabilization with set point turn rate $\dot{\psi}'_s$. The plant behavior $\delta \rightarrow \dot{\psi}'$ is based on the turn rate law

$$\dot{\psi}' = g_k v_a \delta \quad (22)$$

Note, that the inertial turn-rate sensor (yaw axis) measures the turn rate $\dot{\psi}'_m$ which corresponds to $\dot{\psi}'$ and not $\dot{\psi}$.

2. Outer loop (ψ -controller): ψ_s angle control (related to flight direction). The plant behavior $\dot{\psi}'_s \rightarrow \psi$ is given by

$$\dot{\psi} = \dot{\psi}'_s + \dot{\psi}_{\text{ct}} = \dot{\psi}'_s + \dot{\varphi} \cos \vartheta \quad (23)$$

It should be remarked, that the controller deals with multiple input values $[\psi_s, \dot{\psi}_{\text{ct}}] \rightarrow \dot{\psi}'_s$ where $\dot{\psi}_{\text{ct}}$ involves further quantities given by (14). However, it is appropriate to assume $\dot{\psi} \approx \dot{\psi}'$ for the initial design and add the crossterm as compensating correction.

3. Guidance: Control flight towards target point. The flight direction is based on wind window position, hence the guidance computes

$$[\varphi_m, \vartheta_m, \varphi_{\text{TP}}, \vartheta_{\text{TP}}] \rightarrow \psi_s \quad (24)$$

The guidance is done by computing the flight direction γ towards a target point and subsequently ψ_s by inverting (16). It should be finally noted, that due to the switching of target points, discontinuities are imposed on ψ_s . As these steps ψ_s should result in well defined and controlled curve flights, a proper shaping has to be performed. In the presented design this is done in the ψ -controller as described in Sect. 7 in detail.

6. Controller for yaw rate $\dot{\psi}'$

The complete setup of the $\dot{\psi}'$ -controller is shown in Fig. 9. The controller is based on the feedforward and feedback parts marked by the dashed gray boxes. The plant behavior is based on the turn-rate law, compare (22)

$$\dot{\psi}' = g_k v_a \delta \quad (25)$$

In order to obtain a linear plant behavior with stationary parameters, the dependence on v_a is eliminated by the $1/K_{\dot{\psi}}$ block in the feedback controller with $K_{\dot{\psi}} = g_k v_a$. This creation of a meta-actuator is based on the assumption, that $K_{\dot{\psi}}$ changes slowly compared to the $\dot{\psi}'$ dynamics. Due to the proportional nature of the linearized plant ($\dot{\psi}' = K_{\dot{\psi}} \delta$), a PI-controller is used for the control task in addition with a low-pass to suppress unwanted frequency components. Further, a limiter is applied to the error signal ψ_e for safety reasons. It should be mentioned

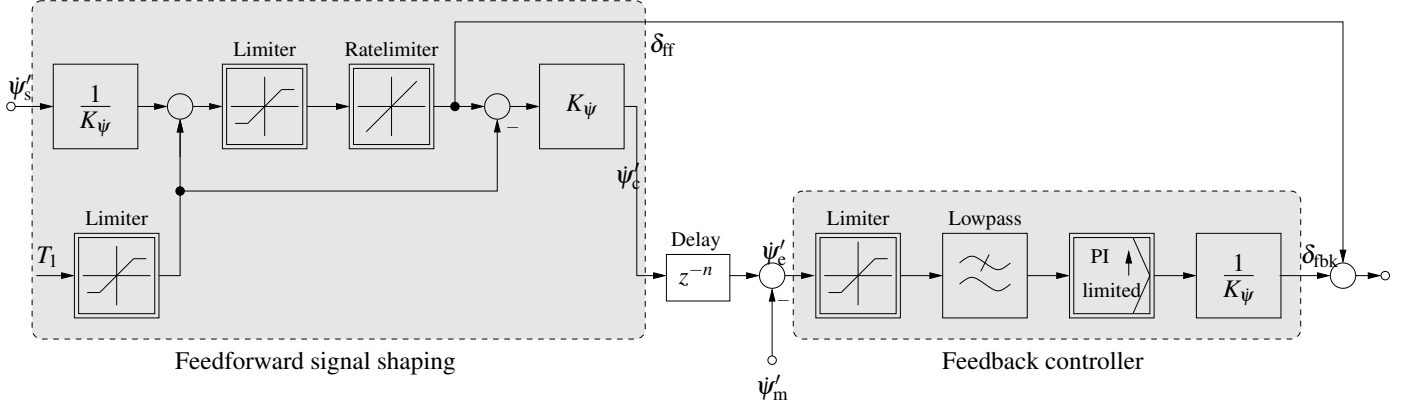


Figure 9: Setup of the ψ -controller based on a feedforward and feedback structure. The limiter and rate limiter in the feedforward shape the signal according to limited steering range and speed of the actuator in the control pod. Note the $1/K_\psi$ -block in order to obtain a linear plant behavior.

here, that the source of the turn rate measurement ψ'_m is a single inertial turn-rate sensor aligned in yaw axis of the flying system.

The feedforward command is computed based on $\delta_{ff} = \psi'_s$ and shaped by a limiter and rate limiter, in order to take into account the limited deflection range and steering speed of the control pod, respectively. It should be mentioned, that gravity leads to an additional term in the turn-rate law, which reads [9, 14]

$$\dot{\psi}' = K_\psi \delta + M \frac{\cos \theta_g \sin \psi_g}{v_a} \quad (26)$$

with a system weight-dependent parameter M . Note, that the angles θ_g and ψ_g are defined with respect to a different coordinate system. For details on definition and origin, the reader is kindly referred to [9, 14]. In order to compensate for the gravity term, the quantity

$$T_1 = \frac{M \cos \theta_g \sin \psi_g}{K_\psi v_a} \quad (27)$$

can be fed into the feedforward block. It should be noted, that the T_1 input feature is given for sake of completeness only. For usual operating conditions, the gravity compensation could be switched off ($T_1 = 0$) and the neglected effect in the feedforward path is easily dealt with by the feedback path. In addition, as M depends on the weight of the flying system, a dependence on l should be taken into account. The accurate compensation of this term, taking into account varying line lengths, is subject of current research and will be published elsewhere.

7. Controller for yaw angle ψ

The complete setup of the ψ -controller is given in Fig. 10. Like the inner loop controller described in the previous section, it features a feedforward/feedback structure. As the plant dynamics, apart from the crossterm correction, is of integrator type, the feedback is implemented as a proportional controller with preceding low pass filter and limiter for safety reasons.

The feedforward part is more involved, since it has to meet the following requirements. As already introduced, the switching of target points imposes steps on the set value ψ_s . These

step discontinuities are related to commanded changes of flight direction and thus have to be implemented as properly curved flights, which should take into account limits on steering deflection δ_s and steering speed $\dot{\delta}_p$. The resulting flown curve radii must be small enough for efficiency reasons and for a safe fitting into a limited space of the wind window. In addition, the crossterm correction $\dot{\psi}_{ct}$ has to be considered according to (23). The shaping of ψ_s could be done by a low-pass filter [12]. However, in order to get time-optimal trajectories for ψ_s meeting the given constraints, an internal loop is implemented, which will be discussed in the following.

The control pod is modeled by a limiter and a rate limiter for steering deflection limit δ_s and steering speed $\dot{\delta}_p$, respectively. The integrator implements $\psi_c = \int dt (\dot{\psi}_{ff} + \dot{\psi}_{ct})$, which reflects the plant dynamics, compare to (23). The scaling from rates to steering and back is done by the $1/K_\psi$ and K_ψ blocks, respectively. The feedback scaling function $f(x)$ implements the inverse of the modeled plant in order to achieve time optimal following of $\psi_c \rightarrow \psi_s$. In order to determine $f(x)$, the process starting with an initial deflection $\delta_i > 0$ and steering with speed $-\dot{\delta}_p$ to a target deflection δ_t is considered. At target deflection, attainment of set point is assumed, i.e. $\psi_c = \psi_s$ and $\dot{\psi}_c = \dot{\psi}_s$. The latter implies

$$K_\psi \delta_t + \dot{\psi}_{ct} = \dot{\psi}_s \quad (28)$$

Inserting the steering $\delta_t = \delta_i - \dot{\delta}_p t$ and resolving w.r.t. t yields:

$$t = \frac{\delta_i - (\dot{\psi}_s - \dot{\psi}_{ct})/K_\psi}{\dot{\delta}_p} \quad (29)$$

The corresponding $\Delta\psi$ of this process can be computed as

$$\Delta\psi = \int_0^t dt' K_\psi (\delta_i - \dot{\delta}_p t') \quad (30)$$

and inserting (29) yields

$$\Delta\psi = \frac{(\delta_i + \dot{\psi}_{ct}/K_\psi)^2}{2\dot{\delta}_p} \quad (31)$$

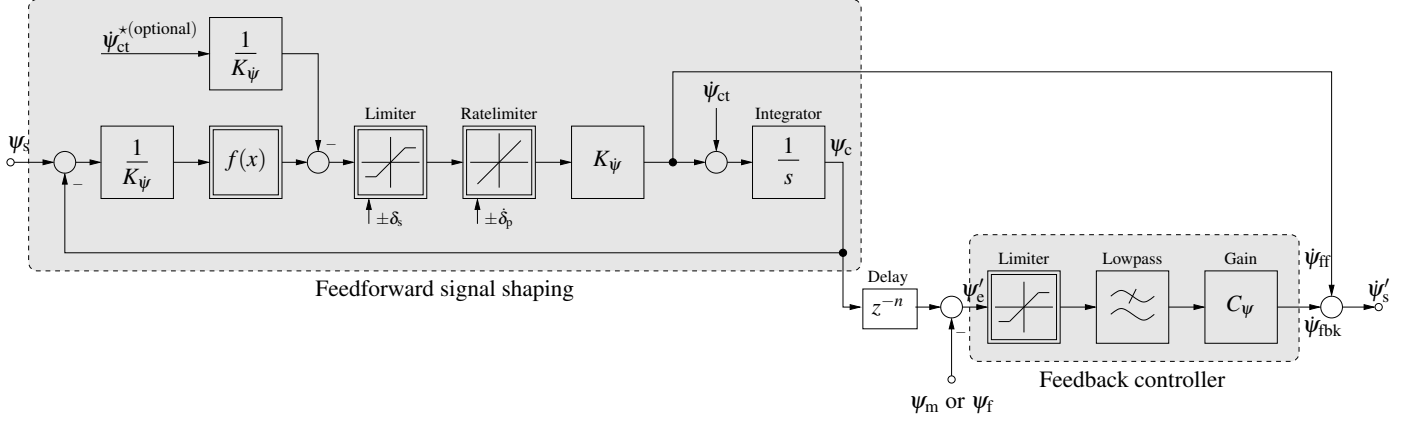


Figure 10: Setup of the psi-controller as feedforward / feedback parts. The feedforward block features an internal loop and is capable of shaping step-wise ψ_s input signals taking into account the given limitations of steering range and speed of the control pod actuator.

This $\Delta\psi$ is interpreted as error, resolving this equation w.r.t. δ_i and reads

$$\delta_i = \sqrt{\frac{2\dot{\delta}_p \Delta\psi}{K_\psi}} - \frac{(\dot{\psi}_{ct} - \dot{\psi}_s)}{K_\psi} \quad (32)$$

As δ_i is deflection related to this error, it is an appropriate feedback value. Comparing (32) to the diagram and generalizing by consideration of $\delta_i < 0$ results in the following

$$f(x) = \text{sign}(x) \sqrt{2\dot{\delta}_p |x|} \quad (33)$$

For constant or step-wise ψ_s input signals, one would chose

$$\dot{\psi}_{ct}^* = \dot{\psi}_{ct} \quad (34)$$

For ψ_s inputs based on target points, $\dot{\psi}_{ct}^* = 0$ is the appropriate choice as can be reasoned as follows: when heading to a target point and the final course is reached, the motion could be regarded approximately as free 'inertial' motion, which implies, compare (12) and text below, $\dot{\psi}_s \approx \dot{\psi}_{ct}$. Inserting into (34) implies $\dot{\psi}_{ct}^* = 0$.

8. Flight direction control

As already introduced, pattern generation is accomplished by navigating towards target points. The basic principle is sketched in Fig. 11. Based on the great-circle navigation, which determines the shortest connection between two given points on the sphere, the direction from the current position φ_m, ϑ_m to the target point $\varphi_{TP}, \vartheta_{TP}$ can be computed by

$$\gamma_s = \arctan\left(\frac{\sin(\varphi_m - \varphi_{TP})}{\cos \vartheta_m \cos(\varphi_{TP} - \varphi_m) - \cot \vartheta_{TP} \sin \vartheta_m}\right) \quad (35)$$

Having determined the flight direction γ_s , the set value for ψ_s is computed by inversion of (17).

In order to perform a curve flight, the target point is switched, as from TP1 to TP2 in this example. This switching leads to a step in ψ_s . However, due to the shaping in the ψ -feedforward as explained in Sect. 7, a smooth and well-controlled curve will

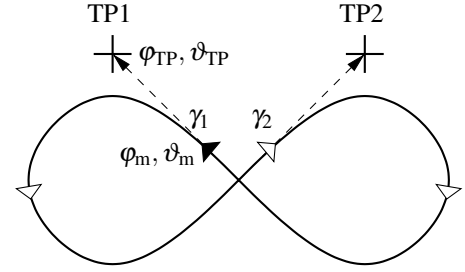


Figure 11: Pattern generation by heading towards target points. Clockwise change of direction in this view is defined as increase of γ .

be commanded. The nominal steering deflection value δ_s determines the radius of the curve, which can be estimated by comparing the approximation for the tangential speed $\dot{\psi}_m' \approx v_a / r_{\text{curve}}$ with (25)

$$r_{\text{curve}} = \frac{1}{g_k \delta_s} \quad (36)$$

Finally, the issue of unwrapping the course angles shall be explained. Using (36) one would obtain for the directions in Fig. 11 e.g. $\gamma_1 = 1.0 \text{ rad}$ and $\gamma_2 = -1.0 \text{ rad}$, respectively. However, the curve $\gamma = 1.0 \rightarrow (-1.0)$ would be clockwise and not counter-clockwise as needed for the drawn figure-eight. Hence $\gamma_2 = (2\pi - 1.0)$ has to be chosen. Alternatively, the same figure could be parameterized by $\gamma_1 = (-2\pi + 1.0)$ and $\gamma_2 = -1.0$. The modulo- 2π offset could be freely chosen as initial condition, but has to be kept constant during pattern operation.

9. Cycle control

In this section, the flight control generating the pattern-eight as well as steering the kite during the return phase is presented. In order to illustrate the target point method, projections of the flight trajectory on the unit sphere including target points are shown in Fig. 12.

The general principle of the target points is basically to control the flight direction heading towards an active target point.

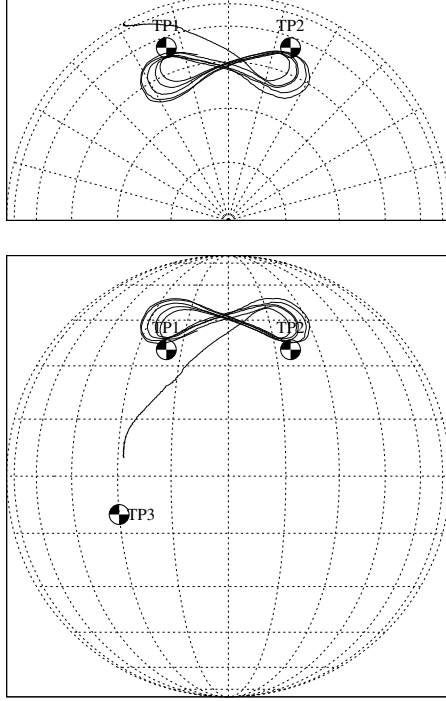


Figure 12: Projection of the flight trajectory on the unit sphere, horizontal view in wind direction (upper figure) and top view (lower figure). Shown are power and transfer phase. Note, that the varying tether length is not represented here. The indicated coordinate grids correspond to a spherical coordinate system with symmetry axis aligned in wind direction.

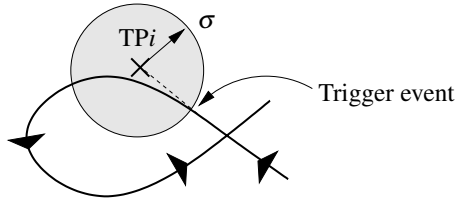


Figure 13: Trigger condition. The active target point is switched to a subsequent target point, when the 'angular' distance on the unit sphere drops below a certain threshold as indicated by the gray circle.

The dynamic pattern is generated by switching to another target point before the currently active target point is reached. The eight-down for the power phase is guided by the two target points TP1 and TP2, compare Fig. 12, with the coordinates chosen symmetrically with respect to the vertical axis as follows: $\varphi_{TP2} = -\varphi_{TP1}$ and $\vartheta_{TP2} = \vartheta_{TP1}$. The trigger condition for switching to the subsequent target point is defined with respect to the 'angular' distance on the unit sphere as follows:

$$(\varphi_m - \varphi_{TPi})^2 \sin^2 \vartheta_{TPi} + (\vartheta_m - \vartheta_{TPi})^2 \leq \sigma^2 \quad (37)$$

This condition is graphically illustrated in Fig. 13. The value σ has been chosen empirically and kept constant for the results presented here. However, in order to optimize the pattern, a dependence $\sigma = \sigma(l)$ could be introduced.

For the transfer and return phases, the kite is flown towards target point TP3, compare Fig. 12. In contrast to the power phase, no switching is performed during these phases. In order

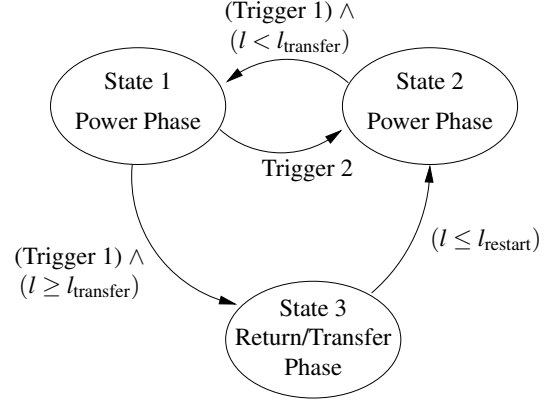


Figure 14: State diagram for the overall cycle control. During the power phase, switching between the target points TP1 and TP2 is based on geometrical trigger conditions, compare Fig. 13. Activation of the Transfer phase is triggered above a maximal line length $l_{transfer}$, in addition to the geometric condition. The return phase is ended below $l_{restart}$.

to get a reasonable feedback, the target point should not be chosen too far away. In addition, it has to be made sure, that the target point is never reached, since the flight direction would become undefined due to the singularity there, compare (36). Hence its elevation value is chosen dynamically dependent on the current position

$$\vartheta_{TP3} = \max(\pi/2, \vartheta_m + \Delta\vartheta) \quad (38)$$

with a typical value $\Delta\vartheta = 0.3$ rad. The azimuth coordinate has to be chosen as a compromise. For $\varphi_{TP3} = 0$, no influence of gravity on the steering behavior would be present, compare (26), but the tether tension would be maximally reduced by gravity. For values $\varphi_{TP3} > 0$, the influence of gravity on tether force is reduced allowing for lower operational wind speeds, but the effect of gravity on steering increases and sufficient space above the surface has to be left for the maneuvers. As a consequence, the chosen value is typically $\varphi_{TP3} = 0.4$ rad.

The complete state diagram for the overall cycle control is shown in Fig. 14. Note, that during the power phase, switching of target points is triggered by geometrical conditions while begin and end of the transfer/return-phases are determined by line length limits, which are in this case $l_{restart} = 130$ m and $l_{transfer} = 270$ m. Finally, it should be remarked that the transition from states 1 to 3 is due to the assumption $\varphi_{TP3} > 0$. The according diagram for negative values $\varphi_{TP3} < 0$ follows straight forward from symmetry considerations.

10. Winch control and power generation

First it should be remarked, that the setup of an electrical motor/generator attached to a frequency converter involves internal control loops, which are not subject to this paper as they have been tuned according to the respective user manuals. However, one feature is worth mentioning. The current control loop of the frequency converter is used to limit the maximal tether load and avoid overload of the kite by setting the maximal current accordingly. This is a very effective mechanism, as the current

control loop is very fast and therefore, apart from inertia effects of the moving elements of winch and motor/generator, depowering is done as fast as possible.

The following section focuses on computing the set value for the winch speed v_{winch} in order to operate efficient power cycles.

It should first be noted, that a computation of the winch speed for optimal power output calls for solving an optimization problem considering complete power cycles, which is quite involved and subject to current research activities [23], [22]. However, these extended models are far beyond the scope of getting a small-scale prototype setup operational in order to prove, that fully automatic power generation is feasible. Hence, simpler approaches are needed, which compute the winch speed based on the system state as e.g. given in [24], which proposes a feed-forward implementation for constant force.

The main idea is to separate flight and winch control on the kinematic level. This is accomplished by flying the pattern geometrically, e.g. guided by target points defined on the unit sphere as primary control and commanding the winch speed dependent on the current pattern. This is also the control strategy chosen when operating the prototype by two human operators. The pilot flies the pattern-eight and static positions, respectively, while the winch operator commands the winch speed accordingly. This task comprises basically winching out during the pattern and winching in during the static flight position, respectively. Hence, the goal is to find simple controllers for the winch speed for the different phases, which will be considered separately in the following. It has to be remarked, that for sake of clarity, only the basic functionalities are given, which were used for the presented experimental results. They may lack robustness w.r.t. untypical wind situations or temporary free (quasi untethered, i.e. a non stretched line) flight. Operational extensions are subject to current development and would go far beyond the scope of this paper.

10.1. Power phase winch control

For the power phase, the thumb-rule using 1/3 of the projected wind speed could be used [1, 2]. Further optimizations have been proposed [25], which suggest a different factor $(1/a) < (1/3)$ by taking into account the return phase. Thus the set point for the winch speed is given by

$$\dot{l}_s = \frac{1}{a} v'_w \cos \vartheta \quad (39)$$

The v'_w value denotes the wind speed at flight position. Note, that v'_w is hardly measurable directly. However making use of (6), which could be regarded as kind of plant $\dot{l} \mapsto v_a$ with

$$v_a = v'_w E \cos \vartheta - \dot{l}_s E \quad (40)$$

and the simple proportional feedback

$$\dot{l}_s = \frac{v_a}{(a-1)E} \quad (41)$$

it can be shown, that this simple loop fulfills the requirement (39) as the stationary value reads $\dot{l} \rightarrow v'_w (\cos \vartheta)/a$.

The setup is drawn schematically in Fig. 15. In order to al-

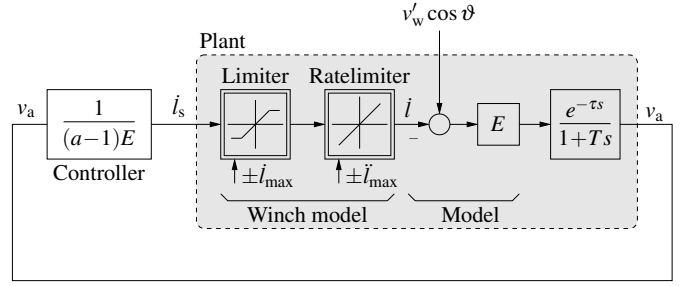


Figure 15: Controller for the power phase based on a proportional feedback of the air path velocity. The wind speed v'_w is the back wind at the flight position.

low for a realistic simulation, the main practical constraints of limited speed \dot{l}_{max} and acceleration \ddot{l}_{max} of the winch as well as delay τ and low pass behavior of the system have been added to the figure, but will not be further discussed here. Note, that due to the loop setup, gusts on v'_w are anticipated by \dot{l} leading to an efficient and consistent behavior of the winch during the power phase.

It should be finally remarked, that winch torque could be used as control variable instead of winch speed by applying a torque set value proportional to the square of the measured winch speed. This leads to quite similar results [28] and could be used alternatively. In addition, winch inertia might play a non-negligible role on system dynamics. The optimization of the winch control system with respect to efficient power cycles is subject to current research activities.

10.2. Transfer and return phase winch control

In view of overall efficiency, winching in as fast as possible at tether forces as low as possible would be desirable. In order to achieve this, *tuning* the glide ratio has been proposed and performance modeling for such systems has been presented [25], [26]. In contrast, our system is operated at *constant* glide ratio, but also allows for low-force return phases as discussed in Fig. 6. In order to understand how to choose the winch speed for efficient transfer and return phases, an optimization problem based on the model of Sect. 4 has been solved.

The simulation, which is sketched in Appendix A, suggests a remarkable simple law for choosing the winch speed \dot{l}_s as function of the windwindow angle ϑ . The simulated results are plotted in Fig. 16. Comparing winch speed and wind window angle, a linear dependence could be suspected which would suggest the following ansatz for the winch controller as given in Fig. 17.

The constant parameters are typically chosen as follows: $\vartheta_0 = 1.05$ rad, $a_{\text{lower}} = -0.55$ and $a_{\text{upper}} = -0.65$. While the a values directly follow from the simulation, the ϑ value can be modified slightly for practical operation in order to take into account line slack during the transfer phase. The winch speed limits are chosen as $\alpha_{\text{limit,in}} = -0.5$ in order to limit the wind window angle to approx. $\vartheta < 1.9$ rad (≈ 110 deg) during the return phase, compare (20). The limit $\alpha_{\text{limit,out}} = 0.3$ is motivated by the rule of thumb given above. For v_w , either the anemometer at the ground station, or a wind estimation algorithm output is used.

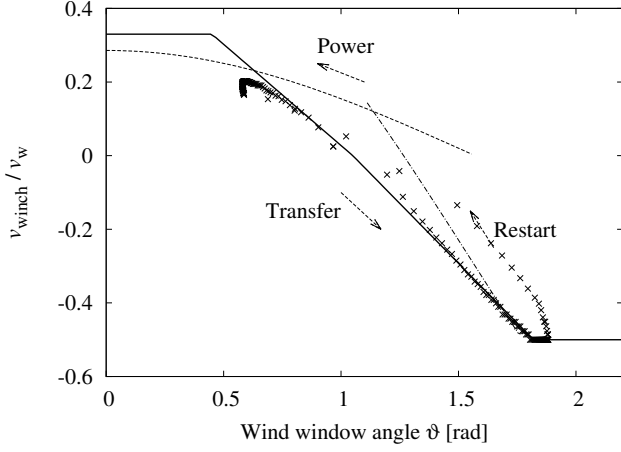


Figure 16: Winch speed as function of windwindow angle. Simulation results of optimized cycles are plotted as points, compare the two middle subplots of Fig. A.22. The data points of the transfer phase could be fitted by a linear saturated transfer function given in Fig. 17 and shown as solid line. For sake of completeness, outputs of the power phase winch controller for $a = 3.5$ (dotted line) and the restart winch controller for $v_{\min} = 1.5v_w$ (dash-dotted line) are given (compare Sect. 10.1 and Sect. 10.3). The whole cycle is operated as indicated by the arrows.

In summary, the winch controller consists of a simple function mapping the wind window angle ϑ_m to v_{winch} , scaled by the wind speed v_w .

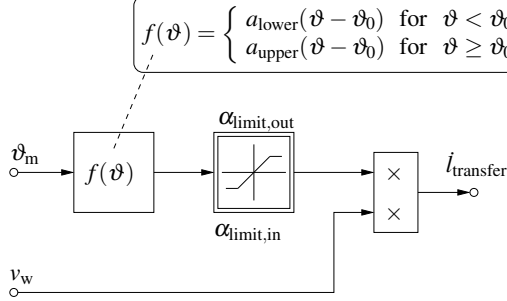


Figure 17: Figure of the winch controller representing the signal flow graphically.

10.3. Pattern restart winch control

A special situation is given while flying from the static windward position heading to target point TP3 back into the dynamical pattern. As the optimization is based on circular orbits, which are quite different to the curve-down maneuver from TP3 to TP1, the simulation results are not suitable for deriving an appropriate control law. First experimental tests have shown, that the transfer phase controller of the previous section can be applied for the restart, albeit the significant force peaks for lower ϑ values should be avoided. The testing of improved controllers is subject to current research activities, a possible restart control phase is drawn in Fig. 16 as dash-dotted line.

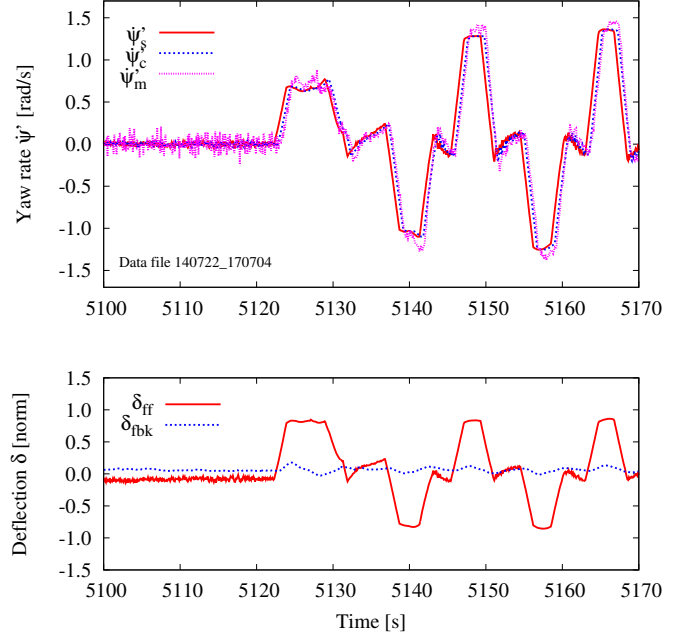


Figure 18: Principle of operation of the ψ' controller illustrated by signals of experimental flight data. Upper plot: comparison of set value ψ'_s (solid), reference value ψ'_c (dashed) and measured value ψ'_m (dotted). Lower plot: feedforward (solid) and feedback (dashed) outputs of the ψ' controller.

11. Experimental flight results

In this section, experimental flight data of the SkySails small prototype, using a 30 m^2 kite at $v_w \approx 8 \text{ m/s}$ wind speed, will be discussed. They should be regarded as first results for a proof-of-concept of the introduced algorithms without claiming the achievement of fully optimized power production cycles.

1. Inner loop (ψ' -controller): Performance results for the inner loop ψ' -controller are given in Fig. 18. In order to review the controller performance, the set (ψ'_s) and reference ψ'_c values for the turn rate are compared to the measured turn rates ψ'_m . The excellent agreement of the measured turn rate shows, that system constraints are met. Note, that the ratio of feedback to feedforward commands is quite small, which indicates, that the feedback is only necessary for correcting small perturbations and uncertainties. This further validates the turn-rate law (25) and (26), on which the feedforward path is based.
2. Outer loop (ψ -controller): The respective controller signals are shown in Fig. 19. Note, that although switching of target points introduces steps to the commanded ψ_s , the output quantity ψ_c is properly shaped subject to limited steering deflection δ_s and speed $\dot{\delta}_p$. An accurate analogy of the estimated orientation ψ_m to the reference value ψ_c can be observed, resulting in the fact, that dynamics is mainly controlled by the feedforward part. Hence, a proper design of the inner loop as well as validity of the dynamics given in Sect. 4.3 can be stated.
3. Guidance: In order to evaluate the flight direction control, the direction to the active target point is compared to the

measured flight direction as plotted in Fig. 20. The measured directions are computed by differences $\Delta\varphi$, $\Delta\vartheta$ between consequent samples using (15), i.e.

$$\gamma_m = \arctan(-\Delta\varphi \cos \vartheta, \Delta\vartheta) \quad (42)$$

For the return phase with insignificant kinematic motion, γ_m becomes more or less undefined and unsuitable as direct control input. In order to handle this issue, a regularization, as proposed in [27, 28], could be used. In contrast, we decided to base the direction control on ψ as introduced in Sect. 4.4. The excellent agreement of directions during the dynamic flight apart from the continuous γ_m following the step in γ_s during curves, demonstrates, that the flight direction control works satisfactorily and relation flights characterized by a step in γ_s and relation (16) between γ and ψ holds.

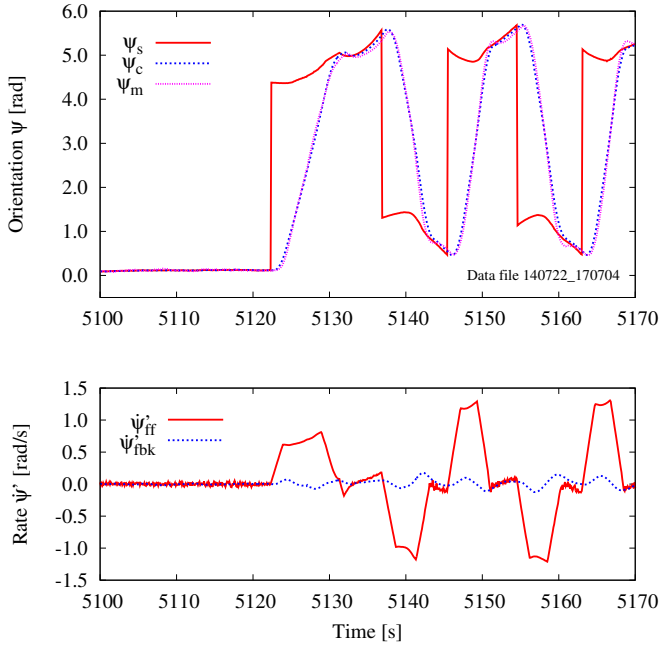


Figure 19: Principle of operation of the ψ controller illustrated by signals of experimental flight data. The commanded ψ_s features steps, which are shaped by the feedforward block to get ψ_c . The measured value ψ_m is shown for comparison.

Finally, this section will be closed with a discussion of experimental power generation data as shown in Fig. 21. As reference value for the generated power, the Loyd's limit is used, which corresponds to a continuous crosswind flight and optimal winch speed for that situation. This limit is calculated assuming, that the airpath speed in crosswind condition is determined by the back wind reduced by winching and the glide ratio as $v_a = E(v_w - \dot{l})$. Using (A.3) and determining the maximum by varying \dot{l} , one finds the above mentioned thumb rule $\dot{l} = v_w/3$ and for the power:

$$P_{\text{Loyd}} = \frac{\rho C_R A}{2} \frac{4E^2}{27} v_w^3 \quad (43)$$

For the flight test conditions $A = 0.7 \cdot 30 \text{ m}^2$, $\rho = 1.2 \text{ kg/m}^3$, $C_R = 1.0$, $E = 5.0$ and $v_w = 7.5 \text{ m/s}$ (estimated at mean flight

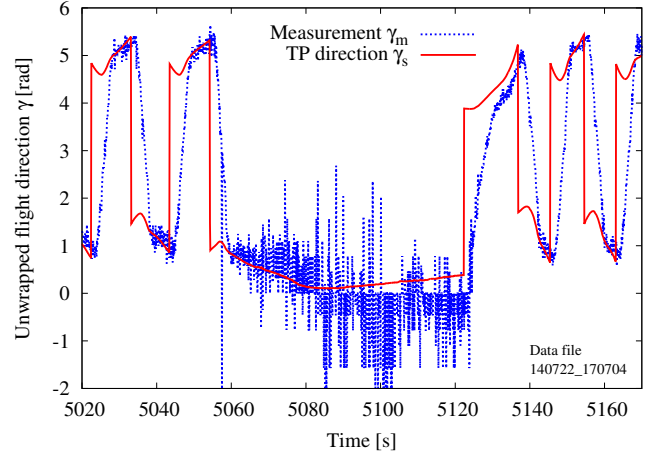


Figure 20: Measured flight directions compared to target point (TP) directions. The noise figure of γ_m originates from the difference equation (42). Note, that γ_m is plotted unfiltered for comparison only and not used for the control. During the return phase, the direction becomes more or less undefined due to the static flight.

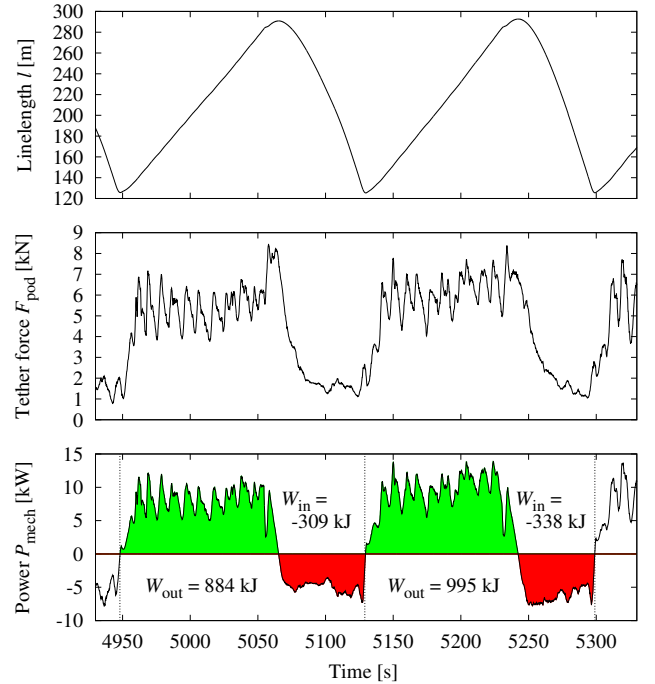


Figure 21: Performance data plot of real flight data at $v_w = 7.5 \text{ m/s}$ (estimation for average flight altitude). The lower subplot shows the mechanical power computed by $P_{\text{mech}} = F_{\text{pod}} \dot{l}$. In order to estimate the electrical net power output, conversion efficiencies have to be taken into account. The energies W_{in} for reeling in and W_{out} are given separately. The average power for the complete cycles is computed by $\bar{P}_{\text{cycle}} = (W_{\text{in}} + W_{\text{out}})/T$ where T is the cycle time. The two plotted cycles yield $\bar{P}_{\text{cycle}} = 3.17 \text{ kW}$ and $\bar{P}_{\text{cycle}} = 3.86 \text{ kW}$, respectively.

altitude), $P_{\text{Loyd}} \approx 19.7 \text{ kW}$ is obtained. Evaluating a typical cycle, as shown in Fig. 21, yields an average power of $\bar{P} = 3.5 \text{ kW}$, hence $\bar{P} = 0.18 P_{\text{Loyd}}$, which is about 75% of the expected value due to simulation results given in Appendix A.

Taking into account, that the simulation does not consider the significant losses due to curve flights and real conditions coming along with gusts, the theoretical simulation based on the simple model and the experimental finding can be regarded as consistent. Hence, although neither precision measurements nor an extended optimization of the power output were in the scope of the presented prototype setup, the presented model as well as the controller setup could be regarded as solid bases for further development steps. Especially the trajectory of recycling back into the power phase, but also the whole power phase are candidates for significant improvements in the near future.

12. Summary and future work

We have presented a complete control setup for autonomous power generation flying tethered kites at constant glide ratio in the pumping cycle scheme. The control structure design is based on and motivated by a simple model for the system dynamics. The discussed flight data with a small-scale demonstrator illustrates, that the implemented target point control allows to fly reliably the pattern eight-down, which is an ambitious scheme, but allows for significantly higher power generation efficiency.

The winch control has been implemented as simple state-feedback and tailored for an efficient transfer phase. Although it is quite rudimentary, it can be utilized during all flight phases with energy generation results not fully optimized but already remarkable.

With respect to future work, there are two major fields for further developments. First, a long-term autonomous operation requires a high level of robustness of the control system under extreme environmental conditions, which basically involve extreme gusts and temporary untethered states. Especially, the development of estimation and filtering algorithms of sensor values is a research field on its own, which has been kept out of this paper in order to focus on the general scheme and control. Extended results will be published elsewhere. Second, it should be noted, that the whole field of optimizing the power output has only been scratched by the surface in this paper. An extended understanding of optimization criteria, which also take into account different wind conditions at different altitudes, has to be established. A further major challenge will arise from the implementation of robust operational algorithms smartly adapting to varying environmental conditions. Currently, only few theoretical proposals [29] and experimental results on that issue have been reported, see e.g. the maximum power point searching stepping algorithm [30], which adapts to varying wind directions.

The final goal of implementing fully autonomous airborne wind energy power plants additionally demands for control systems for starting and landing of the kite. The differences in system dynamics at short tether lengths lead to different control approaches, which are subject to current research activities.

Appendix A. Optimization of power generation cycles

In order to get a principal idea of how to perform transfer and return phases w.r.t. winch speed efficiently with the setup of *constant* glide ratio, a heuristically motivated optimization has been applied to the simple model, which will be briefly presented in the following.

The quantity to optimize is the average power of a complete cycle of duration T

$$\bar{P} = \frac{1}{T} \int_0^T dt \dot{l}(t) F(t) \quad (\text{A.1})$$

using the expression for the tether force

$$F(t) = \frac{\rho}{2} C_R A v_a^2(t) \quad (\text{A.2})$$

with ρ the air density, A the projected kite area and C_R the force coefficient, one obtains for the average power

$$\bar{P} = \frac{\rho C_R A}{2T} \int_0^T dt \dot{l}(t) v_a^2(t) \quad (\text{A.3})$$

As it is reasonable to vary $\psi(t)$ and $\dot{l}(t)$, these are considered as *input functions*. As consequence, a functional $\bar{P} : \{\psi(t), \dot{l}(t), T\} \mapsto \bar{P}[\psi(t), \dot{l}(t), T]$ can be defined by solving the equations of motion (3), (4), (6) and using (A.3). The optimization problem can now be stated:

$$\text{maximize } \bar{P}[\psi(t), \dot{l}(t), T] \quad (\text{A.4})$$

by variation of $\{\psi(t), \dot{l}(t), T\}$ subject to the following constraints:

- Periodic boundaries: $l(T) = l(0)$ and $\psi(T) = \psi(0)$. Further, the initial condition for (3) must also be periodic $\vartheta(0) = \vartheta(T)$.
- There is only one reel-in and one reel-out phase, i.e. $\dot{l}(t)$ has only two roots for $0 \leq t < T$. In addition, the operational range is given, $l_{\min} \leq l \leq l_{\max}$ and these range limits must be reached.
- $\alpha_{\text{limit,in}} \leq (\dot{l}/v_w) \leq \alpha_{\text{limit,out}}$
- $0 \leq \psi(t) \leq \psi_{\max}$, ψ_{\max} and the φ motion is free and not subject to periodic boundary condition through cycles. These condition lead to circular orbits (also below the surface) instead of figure-eights during the power phase. The ψ_{\max} value can directly be regarded as force control as it determines the equilibrium wind window position as discussed in detail in [9]. This rough approximation of figure eights significantly simplifies the optimization algorithm and is adequate for a first approach. Future work should include proper figure eights and consider losses due to curve flights [23].

It should be stated, that the simulation has been performed for $v_w = 10 \text{ m/s}$. Winch speeds for other wind speeds can be easily obtained by scaling the results with v_w accordingly. Simulation curves are shown in Fig. A.22. As a result for the transfer

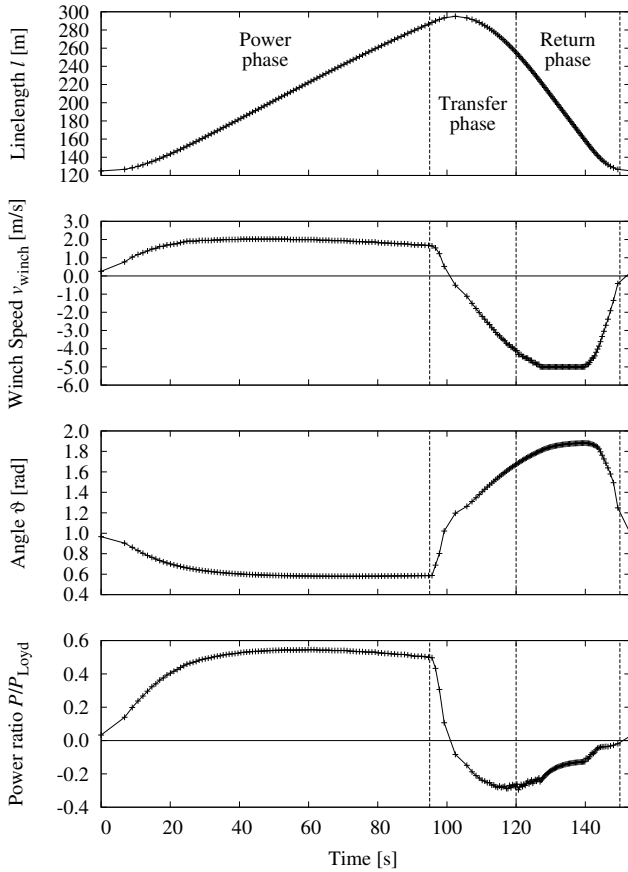


Figure A.22: Optimization results for $v_w = 10$ m/s. The plots comprise one cycle and single phases are separated by vertical dashed lines. The power (lower subplot) is normalized to the Loyd's limit P_{Loyd} , compare (43), and the average value is given by $\bar{P} = 0.24P_{Loyd}$.

and return phase, a similarity of winch speed v_{winch} and angle ϑ can be recognized, which motivates the implementation of a winch controller as linear functions $v_{winch} = v_{winch}(\vartheta)$, compare Fig. 16. Note, that in the first part of the transfer phase the optimization yields $v_{winch} > 0$ and thus suggests utilization of the high tether forces for energy production. Winching in starts for elevation angles higher than $\vartheta_0 \approx 1.05$ rad.

Finally, it has to be remarked, that the results in the appendix have to be considered as a first step in tackling the cycle optimization issue. They should be regarded as illustration of the basic idea rather than a complete treatment of the problem. Hence, further extended investigation of this optimization problem is recommended, which may lead to major modifications of the winch control strategy presented in this paper.

References

- [1] M. L. Loyd, Crosswind kite power, *Journal of energy* 4 (3) (1980) 106–111.
- [2] L. Fagiano, M. Milanese, Airborne wind energy: An overview, in: *American Control Conference (ACC)*, 2012, 2012, pp. 3132–3143.
- [3] U. Ahrens, M. Diehl, R. Schmehl (Eds.), *Airborne Wind Energy, Green Energy and Technology*, Springer Berlin Heidelberg, 2013. doi:10.1007/978-3-642-39965-7.
- [4] M. Diehl, Real-time optimization for large scale nonlinear processes, Phd thesis, University of Heidelberg, Germany (2001).
- [5] A. Ilzhöfer, B. Houska, M. Diehl, Nonlinear MPC of kites under varying wind conditions for a new class of large scale wind power generators, *Int. J. Robust Nonlinear Control* 17 (17) (2007) 1590–1599.
- [6] L. Fagiano, M. Milanese, D. Piga, Optimization of airborne wind energy generators, *Int. J. Robust. Nonlinear Control* doi:10.1002/rnc.1808. URL <http://dx.doi.org/10.1002/rnc.1808>
- [7] J. H. Baayen, W. J. Ockels, Tracking control with adaption of kites, *IET Control Theory and Applications* 6 (2) (2012) 182–191.
- [8] M. De Lellis, R. Saraiva, A. Trofino, Turning angle control of power kites for wind energy, in: *Decision and Control (CDC), 2013 IEEE 52nd Annual Conference on*, 2013, pp. 3493–3498. doi:10.1109/CDC.2013.6760419.
- [9] M. Erhard, H. Strauch, Control of towing kites for seagoing vessels, *Control Systems Technology, IEEE Transactions on* 21 (5) (2013) 1629–1640. doi:10.1109/TCST.2012.2221093.
- [10] C. Jehle, Automatic flight control of tethered kites for power generation, Master thesis, Technical University of Munich, Germany (2012).
- [11] C. Jehle, R. Schmehl, Applied tracking control for kite power systems, *AIAA Journal of Guidance, Control and Dynamics* doi:10.2514/1.62380.
- [12] L. Fagiano, A. Zraggen, M. Morari, M. Khammash, Automatic crosswind flight of tethered wings for airborne wind energy: Modeling, control design, and experimental results, *Control Systems Technology, IEEE Transactions on* PP (99) (2013) 1–1. doi:10.1109/TCST.2013.2279592.
- [13] R. van der Vlugt, J. Peschel, R. Schmehl, Design and experimental characterization of a pumping kite power system, in: U. Ahrens, M. Diehl, R. Schmehl (Eds.), *Airborne Wind Energy, Green Energy and Technology*, Springer Berlin Heidelberg, 2013, pp. 403–425. doi:10.1007/978-3-642-39965-7_23. URL http://dx.doi.org/10.1007/978-3-642-39965-7_23
- [14] M. Erhard, H. Strauch, Theory and experimental validation of a simple comprehensible model of tethered kite dynamics used for controller design, in: U. Ahrens, M. Diehl, R. Schmehl (Eds.), *Airborne Wind Energy, Green Energy and Technology*, Springer Berlin Heidelberg, 2013, pp. 141–165. doi:10.1007/978-3-642-39965-7_8.
- [15] F. Fritz, Application of an automated kite system for ship propulsion and power generation, in: U. Ahrens, M. Diehl, R. Schmehl (Eds.), *Airborne Wind Energy, Green Energy and Technology*, Springer Berlin Heidelberg, 2013, pp. 359–372. doi:10.1007/978-3-642-39965-7_20. URL http://dx.doi.org/10.1007/978-3-642-39965-7_20
- [16] M. Erhard, H. Strauch, Sensors and navigation algorithms for flight control of tethered kites, in: *Control Conference (ECC), 2013 European*, 2013, pp. 998–1003.
- [17] L. Fagiano, K. Huynh, B. Bamieh, M. Khammash, On sensor fusion for airborne wind energy systems, *Control Systems Technology, IEEE Transactions on* 22 (3) (2014) 930–943. doi:10.1109/TCST.2013.2269865.
- [18] M. Ranneberg, Sensor setups for state and wind estimation for airborne wind energy converters. URL [arXiv:1309.1029](http://arxiv.org/abs/1309.1029)
- [19] S. Lucia, S. Engell, Control of towing kites under uncertainty using robust economic nonlinear model predictive control, in: *Control Conference (ECC), 2014 European*, 2014, pp. 1158–1163. doi:10.1109/ECC.2014.6862335.
- [20] P. Williams, B. Lansdorp, W. Ockels, Optimal crosswind towing and power generation with tethered kites, *AIAA Journal of Guidance, Control and Dynamics* 31 (1) (2008) 81–93.
- [21] S. Gros, M. Diehl, Modeling of airborne wind energy systems in natural coordinates, in: U. Ahrens, M. Diehl, R. Schmehl (Eds.), *Airborne Wind Energy, Green Energy and Technology*, Springer Berlin Heidelberg, 2013, pp. 181–203. doi:10.1007/978-3-642-39965-7_10. URL http://dx.doi.org/10.1007/978-3-642-39965-7_10
- [22] G. Horn, S. Gros, M. Diehl, Numerical trajectory optimization for airborne wind energy systems described by high fidelity aircraft models, in: U. Ahrens, M. Diehl, R. Schmehl (Eds.), *Airborne Wind Energy, Green Energy and Technology*, Springer Berlin Heidelberg, 2013, pp. 205–218. doi:10.1007/978-3-642-39965-7_11. URL http://dx.doi.org/10.1007/978-3-642-39965-7_11

- [23] S. Costello, G. Franois, D. Bonvin, Real-Time Optimization for Kites, in: Proceedings of the 5th IFAC-PSYCO Workshop, 2013, pp. 64–69.
- [24] U. Fechner, R. Schmehl, Feed-forward control of kite power systems, *Journal of Physics: Conference Series* 524 (1) (2014) 012081.
- [25] R. Luchsinger, Pumping cycle kite power, in: U. Ahrens, M. Diehl, R. Schmehl (Eds.), *Airborne Wind Energy, Green Energy and Technology*, Springer Berlin Heidelberg, 2013, pp. 47–64. doi:10.1007/978-3-642-39965-7_3.
URL http://dx.doi.org/10.1007/978-3-642-39965-7_3
- [26] U. Fechner, R. Schmehl, Model-based efficiency analysis of wind power conversion by a pumping kite power system, in: U. Ahrens, M. Diehl, R. Schmehl (Eds.), *Airborne Wind Energy, Green Energy and Technology*, Springer Berlin Heidelberg, 2013, pp. 249–269. doi:10.1007/978-3-642-39965-7_14.
URL http://dx.doi.org/10.1007/978-3-642-39965-7_14
- [27] A. Zraggen, L. Fagiano, M. Morari, Retraction phase control using regularized velocity angle, ETH Zurich, Tech. Rep. (TR_ZFM_15103).
URL http://control.ee.ethz.ch/~jaldoz/docs/TechRep/ZFM_TR_151013.pdf
- [28] A. Zraggen, L. Fagiano, M. Morari, Automatic retraction and full cycle operation for a class of airborne wind energy generators, submitted to *Control Systems Technology*, IEEE Transactions on.
URL [arXiv:1409.6151](https://arxiv.org/abs/1409.6151)
- [29] S. S. Diwale, I. Lymperopoulos, C. Jones, Optimization of an airborne wind energy system using constrained gaussian processes, in: *IEEE Multi-Conference on Systems and Control*, no. EPFL-CONF-199717, 2014.
- [30] A. Zraggen, L. Fagiano, M. Morari, Real-time optimization and adaptation of the crosswind flight of tethered wings for airborne wind energy, *Control Systems Technology*, IEEE Transactions on PP (99) (2014) 1–1. doi:10.1109/TCST.2014.2332537.